Flow Turbulence Combust (2012) 89:97–119
DOI 10.1007/s10494-012-9393-0

Analytical and Experimental Study of Pressure Dynamics in a Pulsed Water Jet Device

Sevda Dehkhoda · Michael Hood · Habib Alehossein · David Buttsworth

Received: 29 September 2011 / Accepted: 13 March 2012 / Published online: 29 March 2012

Abstract Pulsed high-velocity water jets are of interest for breaking rocks and other materials. This paper describes a straightforward way of generating single water pulse with a hammer impacting a piston that rests on top of a chamber filled with water. This impacting action pressurises the water, expelling it at high velocity through a nozzle. A theoretical investigation is outlined aimed at gaining a better understanding of this system for generating water pulses. A computational model is developed to simulate the pressure dynamics in the chamber based on continuity and momentum equations for a compressible viscous flow. This model is used to optimise the relative sizes of the hammer and piston as well as the height of the water column to produce the highest velocity water pulse. The model was validated by building an experimental apparatus. In these experiments maximum pressures of about 200 MPa were measured inside the chamber over a time period of about 560 μs. This produced a water pulse with maximum velocity of 600 m/s. Experiments were conducted with nozzle diameters between about 1 mm and 4 mm to study the effect of discharge volume on the pressure history. The results illustrate that although the peak attainable pressure decreases with an increase in nozzle diameter, the duration of the elevated pressure remains similar for all nozzles.

Keywords Pulsed water jet · Compressible fluid · Experimental study · Computational study

S. Dehkhoda (✉) · M. Hood
University of Queensland (CRCMining), St Lucia Campus, Brisbane, Australia
e-mail: s.dehkhoda@uq.edu.au

H. Alehossein
CSIRO, Brisbane, Australia

D. Buttsworth
University of Southern Queensland, Toowoomba, Australia

1 Introduction

Practical methods for producing high-energy water pulses repeatedly have proven difficult. At one extreme are water cannon which provide highly energetic but single pulse impacts on the target [1]. At the other extreme are the very high-frequency low-energy pulsed jets formed using an ultrasonic transducer upstream of the nozzle introduced by Vijay et al. [2] and developed further by Foldyna et al. [3]. Between these extremes are the so-called self-modulated jets. These use an organ pipe structure upstream of the nozzle to induce waves in the flow stream. When these jets exit the nozzle, the air drag causes the continuous jets to break up into a series of pulses as first described by Nebeker and Rodriguez [4] and further developed by Chahine et al. [5]. Few of these systems have found widespread use as a practical device.

Our research set out to understand the production of a single water pulse generated using a water-filled cylindrical steel chamber with a steel piston at one end and a centrally-located nozzle mounted at the other end. In this system the cylinder axis is vertical with the nozzle at the bottom and the piston resting on the water surface. The water pulse is generated when a hammer was used to impact the piston (Fig. 1).

Other workers have conducted similar studies [6–9] but focusing at much higher velocity ranges. In particular Rehbinder [10] developed an analytical model to calculate the stress waves travelling in the piston and the hammer and he validated his model (Fig. 2) using an experimental apparatus not unlike that illustrated in Fig. 1.

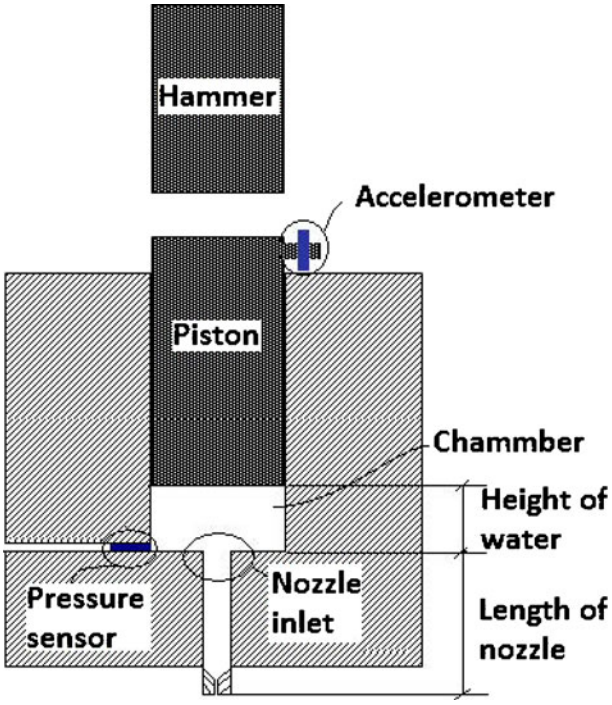

Fig. 1 Schematic view of the water filled chamber, the piston and hammer (not to scale)

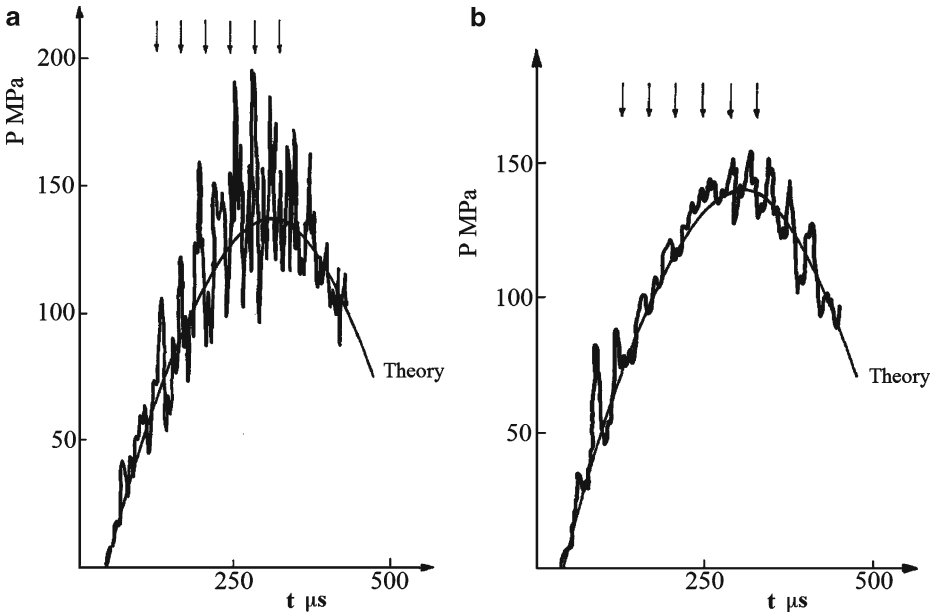

Fig. 2 *Solid line*: pressure profile derived from theory, *oscillating line*: experimental results [10]. **a** and **b** shows higher and lower noise level in the recorded data

2 General Theory for Analytical Model

The goal of the present study was to optimise the design of the hammer, piston and chamber to produce the most energetic and therefore potentially destructive water pulses.

The easiest and most straightforward way to approach the problem is to make two assumptions. First, to treat the piston and the hammer as lumped bodies. This assumption is reasonable since the elastic properties of water and piston differ by two orders of magnitude: $K_w = 2.2$ GPa while $E_p = 200$ GPa. Second, to treat the water column inside the chamber as a spring. This assumption means that the energy delivered from the hammer impact moves the piston forward, compressing and thereby storing energy in the water. As the water approaches the maximum compression, determined by the bulk modulus of water, the piston slows and eventually stops. The compressed water then starts expanding releasing the stored energy and reducing the pressure inside the chamber. Water discharge from the nozzle is initiated as soon as pressure starts to build in the chamber. This model is described in following section.

2.1 Governing equations

The problem to be solved is to calculate the changing water volume in the chamber with a moveable boundary (the piston) and with water discharging through the nozzle. Rehbinder [10] addressed this problem by considering a control volume

inside the chamber and applying the equations of continuity and conservation of mass to relate the movement of the piston to the discharge from the nozzle, assuming that flow inside nozzle and chamber is quasi-steady-state and one dimensional and also that water is inviscid and compressible. In our analysis below a similar approach is adopted, but the non-steady-state aspects of the problem are considered more completely. A comparison of our analysis with that of Rehbinder in the equations that follow is made clear by labelling Rehbinder's equations with the index R.

2.1.1 Compressibility of water

A first approach is to note that the water density can be related to pressure in the chamber using the bulk modulus of water:

$$\mathrm{d}p = K_w \frac{\mathrm{d}\rho}{\rho} \tag{1}$$

where K_w is the bulk modulus of water which is assumed to be constant and equal to 2.2 GPa. In reality however, the bulk modulus varies with pressure. An alternative method for relating the density of a compressible fluid to pressure is via the Tait equation of state [6, 11, 12] which for water is written as:

$$\frac{P+B}{P_0+B} = \left(\frac{\rho}{\rho_0}\right)^n \tag{2}$$

where, n and B are constants and for water n =7.415 and $B = 296.3$ MPa [12]. The subscript zero denotes the reference condition which here is $P_0 = 0$ and so $\rho = \rho_w$. The Tait equation is an empirical equation of state with some theoretical justification. This equation has been found to provide an excellent representation of the equation of the state of water for pressures up to 2.5 GPa at temperature range of 20°–60°C for $n = 7$ and $B = 321.4$ MPa [11]. However, the application of the Tait equation with these empirical constants for lower pressure values between 10–100 MPa has not led to acceptable results [13]. Different constant values have been determined by different scientists based on their experimental data; the comparisons showed that Tait equation is in error at the low pressure range [14].

Integration of Eq. 1 for initial values of $P = 0$ when $\rho = \rho_w$ (original density of water) results in a state equation for direct comparison with Eq. 2:

$$P = K_w \ln\left(\frac{\rho}{\rho_w}\right) \tag{3}$$

Applying the Tait state equation (2) for $P = 200$ MPa gives a water density of 1072 kg/m^3 whereas using a constant value of K_w equal to 2.2 GPa in Eq. 3 gives a water density of 1095 kg/m^3, a difference in density of 2.1%. Pressures of up to 200 MPa can be reached in the present work, so it is important to accurately model the pressure-density relationship. Therefore, the state equation described by Eq. 3 is adopted for the present work.

Rehbinder [10] adopted an approximate equation of state for water, based on the pressure profiles given by Bridgeman [15] for various relative densities at constant temperatures, since he demonstrated that it is reasonable to neglect the temperature

change during the short event when the water is being compressed. Therefore, Rehbinder [10] assumed an approximated linear relation between pressure, P, and density, ρ, in which the pressure function cannot accept negative values:

$$P = E_{wf}\left(\frac{\rho}{\rho_w} - 1\right) \tag{3R}$$

where E_{wf} is a fictitious term for water compressibility with value of 2.96 GPa. It corresponds to a fictitious speed of sound, C_{wf}, calculated as 1750 m/s for the density of water at atmospheric pressure, $\rho_w = 1000\ \mathrm{kg/m^3}$.

2.1.2 Continuity and conservation of fluid mass

Starting from the well-known Reynolds' transport theorem, in which N_{sys} represents the extensive quantity of any physical property of the fluid (e.g., momentum, energy) and η is the corresponding value per unit mass, the intensive property for any finite control volume of cv bounded by a control surface boundary cs, so that [16]:

$$\frac{\mathrm{d}N_{\mathrm{sys}}}{\mathrm{d}t} = \left(\frac{\partial}{\partial t}\int\int\int(\rho\eta).\mathrm{d}V\right)_{\mathrm{cv}} + \left(\int\int\rho\eta\mathbf{u}_{\mathrm{cs}}.\mathrm{d}\mathbf{A}\right)_{\mathrm{cs}} \tag{4}$$

The equation of continuity or conservation of fluid mass can be derived from Eq. 4 by simply substituting $\eta = 1$, i.e.:

$$\frac{\mathrm{d}m}{\mathrm{d}t} = \left(\frac{\partial}{\partial t}\int\int\int\rho.\mathrm{d}V\right)_{\mathrm{cv}} + \left(\int\int\rho u.\mathbf{n}\mathrm{d}A\right)_{\mathrm{cs}} = 0 \tag{5}$$

in which m is fluid mass, ρ is density, u is velocity, $\mathbf{n}$ is the outward normal to the control surface (cs), A represents the boundary surface and V denotes the volume inside the control volume domain. Equation 5 implies that no fluid mass can be created or destroyed in the control volume. In the rate form, this equation translates into the statement that the rate at which mass accumulates inside the control volume must be balanced by the rate at which it enters and exits across the control surface [16]. Within the chamber volume provided properties are uniform, as a result the rate of change of the accumulated mass inside the control volume for compressible water is simply:

$$\left(\frac{\partial}{\partial t}\int\int\int\rho.\mathrm{d}V\right)_{\mathrm{cv}} = \frac{\partial}{\partial t}(\rho A(h-x)) = \dot{\rho}A(h-x) - \rho A\dot{x} \tag{6}$$

where again, ρ is the density of water, A is the cross sectional area of the chamber, h is the original height of water column in the chamber, x and $\dot{x}$ are the displacement and velocity of the piston. The outflow term is positive in this equation.

While the rate of fluid mass inflow through the control surfaces is zero, the rate of mass outflow through the nozzle and the gap between piston and chamber walls will not generally be zero, so the second term is approximated using a quasi-steady-state approach:

$$\left(\int\int\rho u.\mathbf{n}\mathrm{d}A\right)_{\mathrm{cs}} = c_d\rho ua + \frac{\pi D\ell^3\mathrm{d}P}{12\mu L} \tag{7}$$

The first term on the right hand side is a quasi-steady-state approximation for the volumetric rate of discharge through the nozzle where c_d is the discharge coefficient of nozzle (which, for the nozzle type used in the experiments described below is equal to 0.85), a is the cross sectional area of nozzle exit and u is the instantaneous velocity of discharge at the nozzle exit. The second term on the right hand side of the Eq. 7 is a quasi-steady-state approximation of possible leakage of water through the gap between the piston and the wall of the cylindrical chamber. This is given in terms of volumetric rate (or discharge unit) varying with the pressure drop in the leakage gap flow where this head loss itself is caused by the shear stresses resisting the flow along the both cylindrical wall boundaries [16]. In this term, $\mathrm{d}P$ is the pressure difference along the piston, ℓ is the gap between the piston and chamber wall, D is diameter and L is length of the piston and μ is dynamic viscosity of water.

Combining Eqs. 6 and 7 we have:

$$\dot{\rho} A(h-x) - \rho A\dot{x} + c_d \rho u a + \frac{\pi D \ell^3 \mathrm{d}P}{12\mu L} = 0 \tag{8}$$

Rehbinder [10] assumed the viscosity of the fluid to be zero, $\mu = 0$. As a result, he ignored the leakage discharge term in his model and considered a unit discharge coefficient for his nozzle, i.e. $c_d = 1.0$. Hence, the Rehbinder's version of Eq. 8 relating to conservation of fluid mass reduces to:

$$\dot{\rho} A(h-x) - \rho A\dot{x} + \rho u a = 0 \tag{8R}$$

2.1.3 The conservation of mechanical energy and Bernoulli equation

For the next stage of the analysis, the velocity of flow discharge through the nozzle needs to be determined. The chamber diameter is orders of magnitude greater than the nozzle diameter, typically $A/a = 50$, and if we assume that there is a steady-state flow with no radial flow component in the whole chamber-nozzle system, the axial flow inside the nozzle can be modelled as a one-dimensional flow. In this case, Bernoulli's equation for compressible flow is used to approximate the average velocity of the jet at the nozzle exit from the value of the pressure inside the chamber. Since the water flow velocity inside the chamber is much smaller than the jet velocity at the nozzle exit, the Bernoulli hydrodynamic equation is written only for the nozzle segment where the fluid velocity is considerably higher than that in the chamber segment. In this case, the pressure inside the chamber is treated as the stagnation pressure of the flow that is discharged through the nozzle:

$$\int_P^0 \frac{\mathrm{d}P}{\rho} + \frac{u^2}{2} = 0 \tag{9}$$

where u is discharge velocity at the nozzle exit. The chamber includes some relatively sharp corners and area changes on the path towards the nozzle exit (see Fig. 1) and these can result in shearing and separated flow, which can cause appreciable head losses. This effect has been accounted for by adding a head loss or kinetic energy dissipation term to Eq. 9:

$$\int_P^0 \frac{\mathrm{d}P}{\rho} + \frac{u^2}{2} + k\frac{u^2}{2} = 0 \tag{10}$$

where k is the head loss coefficient. The value of this coefficient for square-edged inlets can be assumed to be 0.5 [16]. Therefore, Eq. 10 can be further simplified to:

$$\int_P^0 \frac{\mathrm{d}P}{\rho} + 1.5\frac{u^2}{2} = 0 \tag{11}$$

Rehbinder's approach to this problem was different. Although he ignored the flow dynamics in the chamber and considered only the inside domain of the nozzle, he added an inertia term instead to include non-steady-state flow in nozzle. His equation for compressible and non-steady-state flow inside the nozzle reads:

$$\int_P^0 \frac{\mathrm{d}P}{\rho} + L_e\frac{\partial u}{\partial t} + \frac{u^2}{2} = 0 \tag{11R}$$

where L_e in this equation was the effective length of the nozzle, $0 < L_e < L$, L being the total length of the nozzle. L_e has been defined using the mean value theorem of the integral calculus in such a way that the acceleration of the water along the nozzle, from the inlet to the exit, could be replaced by the rate of the change of the velocity at the nozzle exit. In other words, if ξ was the distance variable along the nozzle axis and v was the axial component of the velocity variable along the nozzle, the rate of the velocity change along the nozzle length was simplified to:

$$\int_0^L \frac{\partial v}{\partial t}\mathrm{d}\xi = L_e\frac{\partial u}{\partial t} \tag{12}$$

$$L_e = L_0 + \frac{d_e}{d_i}L_i \tag{13}$$

where d_e and d_i are the exit and inlet diameters of the nozzle respectively, L_0 is the straight length of the nozzle (parallel walls) with diameter of d_e, and L_i is the length of it with varying diameter [10].

2.1.4 Hammer and piston dynamics

The following parameters are unknown and need to be determined from the main set of governing Eqs. 3, 8 and 11, to reproduce pressure dynamics inside the chamber: $x(t)$ and $\dot{x}(t)$ are the displacement and velocity of water-piston interface, $\rho(t)$ and $\dot{\rho}(t)$ are the water density and its temporal derivative, $P(t)$ and $u(t)$ are the pressure in the chamber and the velocity of discharge at the nozzle exit. Further equations are required in order to solve the problem and these equations can be developed by considering the dynamics of the piston.

Since both the hammer and the piston are treated as lump bodies, the initial velocity of the piston-water interface, $\dot{x}(0)$, is equal to the velocity of piston at its centre of mass immediately after impact. During the collision the equation of momentum in the axial direction can be written as:

$$M_p.V_{p,1} + M_h.V_{h,1} = M_p.V_{p,2} + M_h.V_{h,2} \tag{14}$$

In this equation M and V are mass and velocity while the p and h indices denote piston and hammer, respectively. Further, subscript 1 refers to the approach before the impact and subscript 2 indicates the separation after impact.

During the impact of the hammer and piston some of the kinetic energy delivered by the hammer is dissipated due to the local plastic deformation on contact surface of piston and the generation of heat, sound and internal friction. If the internal friction is ignored this energy dissipation can be taken into account using the coefficient of restitution, C_r, which is simply the ratio of the relative separation velocity to the relative approach velocity, i.e.:

$$C_r = \frac{V_{p,2} - V_{h,2}}{V_{p,1} - V_{h,1}} \tag{15}$$

If the coefficient of restitution is zero, the relative separation velocity is zero and the impact is perfectly plastic. If the coefficient of restitution is unity, the relative separation velocity equals the relative approach velocity and the kinetic energy of the system is preserved. This situation is the case of perfectly elastic impacts [17].

If the value of the coefficient of restitution is known or assumed, the final velocity of hammer and piston after impact can be determined from the momentum conservation Eq. 14. Therefore, we can calculate separation velocities of the hammer and the piston as below:

$$V_{p,2} = \frac{(C_r + 1) M_h V_{h,1} + V_{p,1}(M_p - C_r M_h)}{M_p + M_h} \tag{16}$$

$$V_{h,2} = \frac{(C_r + 1) M_p V_{p,1} + V_{h,1}(M_h - C_r M_p)}{M_p + M_h} \tag{17}$$

The assumption of a lump hammer and piston implies an instantaneous collision between the hammer and the piston [18]. Therefore, immediately after impact, the velocity of the piston will be equal to its separation velocity, $\dot{x}(0+) = V_p(0+)$; $\dot{x}(t)$ and $x(t)$, the velocity and displacement of the water-piston interface can be determined using the equation of motion or Newton's second law. The model assumes that as the piston moves forward it compresses the water causing the pressure to rise. The rising pressure resists the motion of the piston and reduces its velocity. This resistant force is proportional to the instantaneous pressure inside the chamber and can be determined as a function of the acceleration of the piston using Newton's second law:

$$F(t) = -P(t) A_p = M_p \ddot{x}(t) \tag{18}$$

where $F(t)$ is the resistant force applied on the piston by the water, $P(t)$ is the instantaneous pressure in the chamber, $\ddot{x}(t)$, M_p and A_p are, respectively, the instantaneous acceleration, mass and cross sectional area of the piston. First integration of Eq. 18 leads to the velocity equation and second integration yields the displacement equation of the piston as below:

$$\dot{x}(t) = -\frac{A_p}{M_p} \int_0^t P(t) \mathrm{d}t + \dot{x}(0) \tag{19}$$

$$x(t) = -\frac{A_p}{M_p} \int_0^t \left(\int_0^t P(t) \mathrm{d}t \right) \mathrm{d}t + \dot{x}(0) t \tag{20}$$

where $\dot{x}(0)$ is the piston velocity immediately after impact and can be determined using Eq. 16 based on the impact velocity of the hammer and a coefficient of restitution, C_r, of 0.65 for steel.

The discharge velocity at the nozzle exit is determined as a function of the pressure inside the chamber by the integration of Eq. 11 using the state equation described in Eq. 3:

$$u(t) = \sqrt{\frac{2K_w}{1.5\rho_w}\left(1 - \exp\left(-\frac{P(t)}{K_w}\right)\right)} \tag{21}$$

Consequently, placing Eqs. 3, 19, 20 and 21 in Eq. 8, gives the chamber pressure as:

$$\frac{\mathrm{d}P}{\mathrm{d}t} = \left\{K_w\left(A_p\left(-\frac{A_p}{M_p}\int_0^t P(t)\mathrm{d}t + \dot{x}(0)\right) - c_d a\sqrt{\frac{2K_w}{1.5\rho_w}\left(1 - \exp\left(-\frac{P(t)}{K_w}\right)\right)}\right)\right.$$
$$\left. - \frac{\pi D\ell^3 \mathrm{d}P}{12\mu L}\exp\left(-\frac{P(t)}{K_w}\right)\right\} / A_p\left(h - \left(-\frac{A_p}{M_p}\int_0^t\left(\int_0^t P(t)\mathrm{d}t\right)\mathrm{d}t + \dot{x}(0)t\right)\right) \tag{22}$$

Equation 22 was solved for $P(t)$ using the Runge–Kutta–Fehlberg numerical solution method with time steps, dt, of 0.1 microsecond using a computer program developed in Visual Basic.

2.2 Model results

The model, Eq. 22, was solved for different combinations of the hammer and piston masses in order to find the optimal combinations of masses keeping the nozzle diameter and the water column height unchanged. The resultant pressure profiles for these different runs are illustrated in Fig. 3. Figure 3a, shows the pressure history graphs, generated in a sequence by increasing the hammer mass whilst keeping the piston mass constant; Fig. 3b presents pressure profiles as the mass of the piston was varied for a constant hammer mass.

The results show that at a constant piston mass the peak pressure rises as the hammer mass increases if the impact velocity remains unchanged. This occurs because the input energy of the system increases with hammer mass. Furthermore,

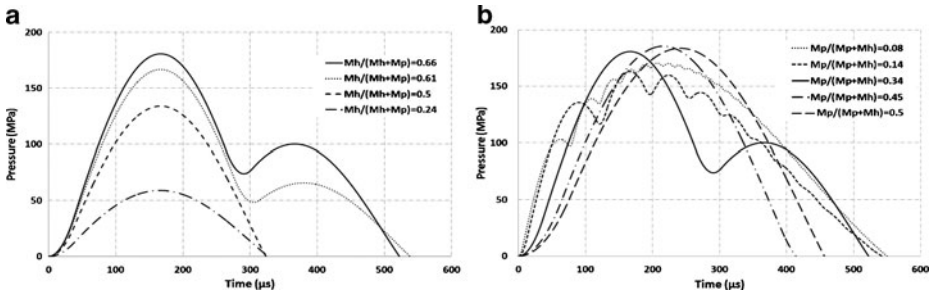

Fig. 3 Elevated pressure profile inside the chamber with different configurations of the hammer and piston masses; **a** constant M_p, change in M_h; **b** constant M_h, change in M_p

the shape of the pressure history changes from a single inverted parabola to a dual inverted parabola as the hammer mass increases. The second parabola is the result of secondary collision between the hammer and the piston. This behaviour is also observed when the hammer mass is kept constant whilst the mass of the piston is varied. As shown in Fig. 3b when the piston mass is much lower than that of the hammer the pressure history is an inverted parabola with superimposed oscillations; the result of multiple impacts between hammer and piston. As the mass of the piston approaches the mass of the hammer, the pressure graph becomes a single inverted parabola indicated a single collision taking place between the hammer and the piston.

The calculated volumes of the water pulses generated with these different configurations of hammer and piston are shown in Fig. 4. As can be seen, the largest pulses correspond to the greatest hammer mass. However, there is no similar correspondence between the pulse volume and the piston size. From Fig. 4, the largest pulses correspond to the configurations with ratios of the piston to the total mass $M_p/(M_p + M_h)$ of 0.08, 0.14 and 0.34. Examining the pressure history of these three cases in Fig. 3 shows that the first two, $M_p/(M_p + M_h)$ of 0.08 and 0.14, produce multiple impacts—this is likely to reduce the coherence of the water pulse. Whereas the third case, $M_p/(M_p + M_h) = 0.34$, creates only a double impact and is therefore likely to produce a more coherent pulse. As a result, this combination is chosen for further studies.

Next we use the model to examine the effect of the height of the water column on the history of pressure build-up inside the chamber. The results, Fig. 5, show the high sensitivity of the pressure response to the initial volume of water in the chamber. As the height of the water column increases the maximum pressure decreases and the time over which that pressure acts increases. Since the value of the elevated pressure in the chamber indicates the velocity of the water pulse as it exits the nozzle and the

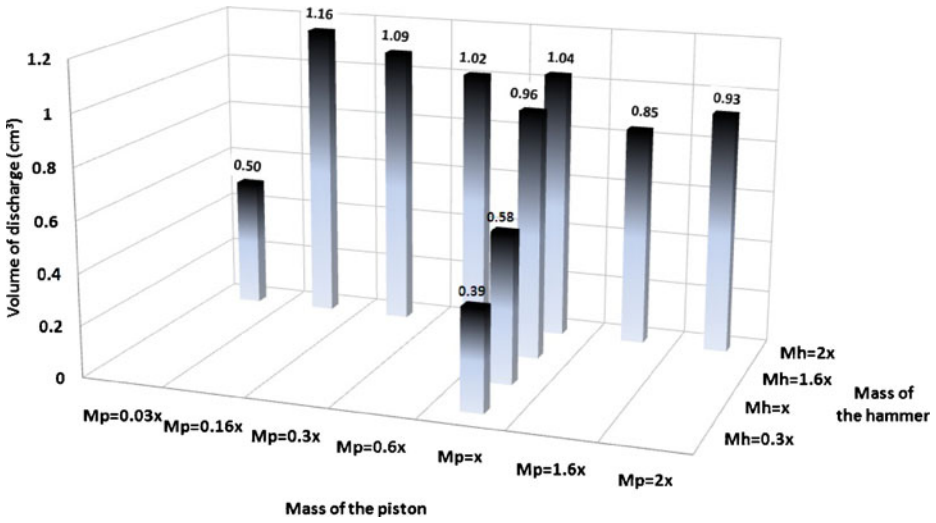

Fig. 4 Volume of the generated water pulses using different masses of hammer and piston, x is randomly selected value (water column height constant)

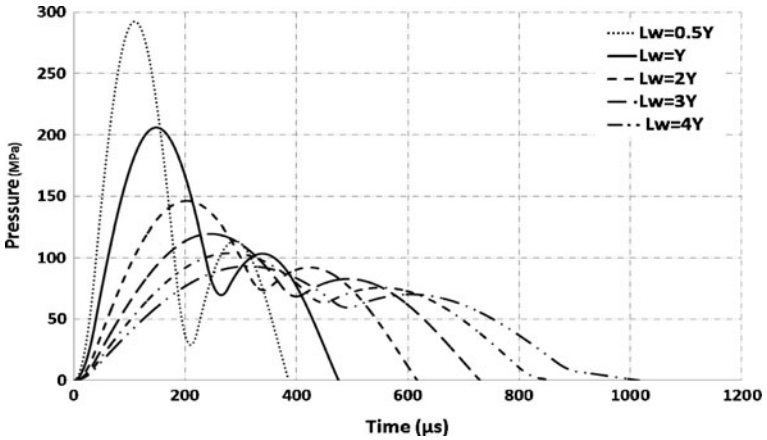

Fig. 5 Pressure history of the chamber for variations in the initial water column heights, L_w, where Y is randomly selected value ($M_h = 2M_p$)

duration of the pressure pulse indicates the pulse length, the model allows the height of the water column to be selected based on the desired capabilities from the system.

3 Design of the Experimental Apparatus

The model was used to design a hammer-piston-chamber system to generate water pulses. Our design differs from the apparatus built by Rehbinder [10]. A comparison of the two systems is given in Table 1.

The results of our model with a quasi-steady-state flow assumption ($\partial u/\partial t = 0$) at the nozzle, for the parameters listed under Present Design in Table 1, are illustrated in Fig. 6. This figure compares the pressure history inside the chamber using different nozzle sizes. The first peak pressure is the greatest (200 MPa) for a blocked chamber (nozzle diameter of zero) and is the lowest (165 MPa) for the 4.02 mm nozzle diameter.

The second peak pressure as well as the minimum pressure between these two peaks follows the same pattern (largest for the blocked chamber and lowest for the 4.02 mm nozzle). The smaller the nozzle size, the higher the pressure. However, the ratios of the two peak pressures to the minimum pressure value (between these two

Table 1 Comparison of Rehbinder's with the present design

Factor	Rehbinder's design	Present design
Diameter of water chamber, mm	107.2	50
Height of water in chamber, mm	26.5	13
Length of hammer and piston, mm	320	195
Mass of hammer, kg	22.7	6.1
Mass of piston, kg	22.7	3.2
Impact velocity of hammer, m/s	7.67	10.85
Input energy to system, J	668	359

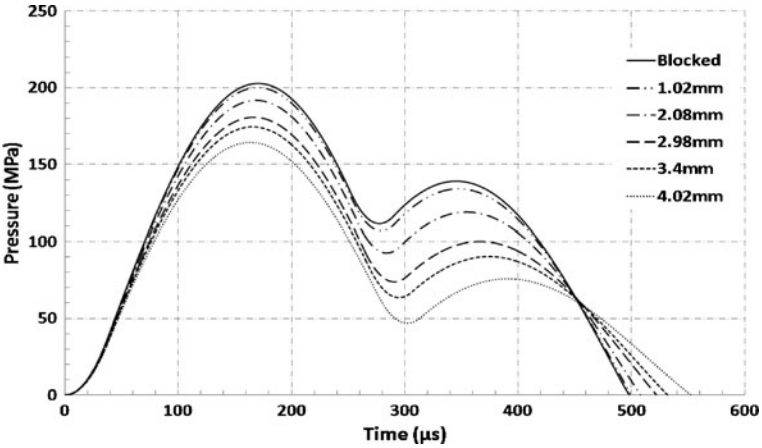

Fig. 6 Pressure history inside the chamber for different nozzle sizes- analytical model for steady-state flow

peaks) vary with nozzle diameter, Fig. 7. These ratios are the largest for 4.02 mm nozzle and decrease as the nozzle size decreases. The higher this ratio, the greater the disturbance to the flow through the nozzle, and hence, presumably the less the coherence of the emerging water pulse.

The time duration of the elevated pressure inside the chamber also varies with nozzle size. The longest duration of 550 μs is for the 4.02 mm nozzle while the shortest duration belongs to the blocked chamber and is about 500 μs.

The calculated pressure history inside the chamber for a 1.02 mm nozzle is shown in Fig. 6. Comparing this with the pressure history inside Rehbinder's chamber with the same size nozzle (Fig. 2) shows great potential for improving the capability of system. The maximum attainable pressure with Present Design system is 200 MPa, 30% higher than the maximum attainable pressure (140 MPa) with Rehbinder's equipment, whilst the input energy of our system is almost half that of Rehbinder, see Table 1. The duration of the pulses produced with both systems cannot be compared as Rehbinder did not provide a full history of the pressure changes.

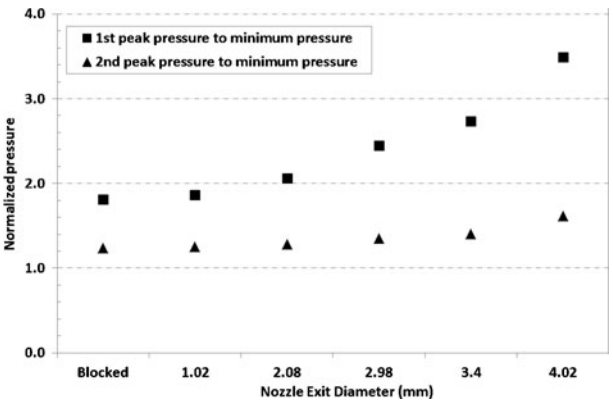

Fig. 7 Variation of the ratios of 1st and 2nd peak pressure to the minimum pressure with Nozzle diameter

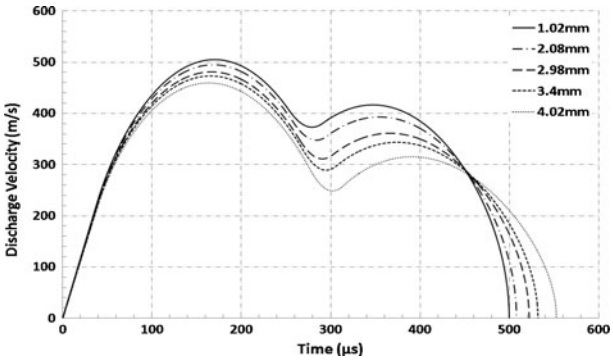

Fig. 8 Discharge velocity history at nozzle exit for different nozzle sizes-analytical model for steady-state flow

Figure 8 compares the calculated velocity of discharge at the nozzle exit for all five of the nozzle sizes examined. These graphs follow the same pattern as the pressure histories.

Knowing the velocity of discharge at the nozzle exit allows the instantaneous volume of the water ejected from nozzle to be easily determined by multiplying the cross sectional area and nozzle discharge coefficient at the corresponding velocity values. As an example Fig. 9a illustrates the volumetric flow rate at the exit of the 2.98 mm diameter nozzle. The area under this profile indicates the total volume of the generated pulse after impact. For the 2.98 mm nozzle diameter this was 1.04 cm^3.

The total volume of discharge for different nozzle sizes is shown in Fig. 9b. Perhaps unsurprisingly, this volume increases as the nozzle diameter increases. As a result the total energy of the generated water pulse increases with nozzle exit diameter even though the velocity of discharge decreases. The total energies of generated water pulses are summarised at Fig. 10.

4 The Experimental Apparatus

The described model was used to design an efficient piston, hammer and chamber system, Table 1. The hammer was dropped from a height of 6 m onto a piston that initially was resting on the surface of a water-filled cylindrical chamber. The

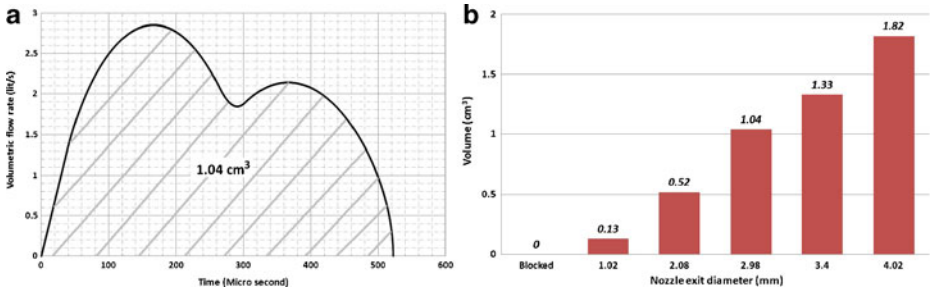

Fig. 9 **a** Discharge volume history from 2.98 mm nozzle; **b** Calculated discharge volume for different nozzle sizes

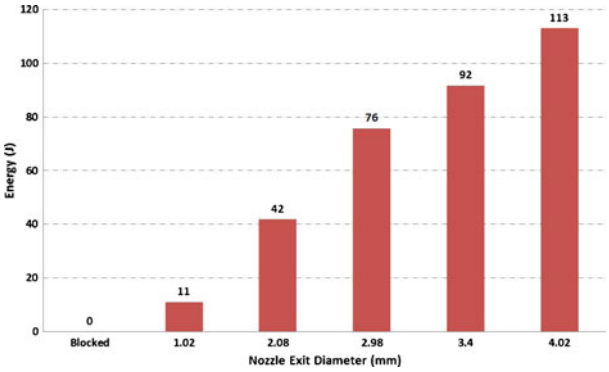

Fig. 10 Energy of generated water pulses using different nozzle sizes

chamber had a nozzle centrally mounted in the cylinder end opposite to the piston as illustrated in Fig. 1. The nozzle head was covered with a tape to prevent the water inside the chamber from leaking out prior to the hammer impact. All of the components of the system were supported on a rigid steel frame.

A dynamic pressure sensor (manufactured by PCB Piezotronics, model 109C11) was mounted flush on the inside wall of the chamber (see Fig. 1) to record the pressure history during the impact event. Data acquisition was accomplished using the pressure transducer, a signal conditioner, an oscilloscope and a laptop. The data were digitised at a 2.5 MHz sampling rate and the computer software LabVIEW was used for processing and displaying the signals.

The transfer of energy from the hammer to the piston and consequently the velocity of piston after impact depends on the quality of impact. The maximum velocity is achieved with coaxial collision between the hammer and the piston. Inevitably any plastic deformation at the contact surfaces of the piston and hammer absorbs some of the energy.

Five nozzles with the same throat diameters used in the modelling described above (d = 1.02, 2.08, 2.98, 3.40, 4.02 mm) were acquired. All other aspects of the internal geometry of these nozzles were identical.

5 Experimental Results

Experiments with each nozzle were repeated to obtain at least 5 reproducible and consistent pressure profiles. For example, Fig. 11a illustrates the pressure history records of the pressure chamber with the 2.98 mm nozzle for 6 acceptable experiments. Three out of a total 9 experiments from this set were disregarded due to inconsistent pressure profiles with large pressure fluctuations shown in Fig. 11b. We consider that these large oscillations were caused by high energy micro-jets produced by the collapse of air pockets that were not expelled from the chamber during refilling. The results of the six approved experiments all have very similar profiles with maximum discrepancy of about $\pm 15 MPa$ within the duration of 550 μs.

Time zero in the recorded profiles was the instant at which the piston starts moving due to impact. This instant was captured using an accelerometer mounted on the piston, Fig. 1.

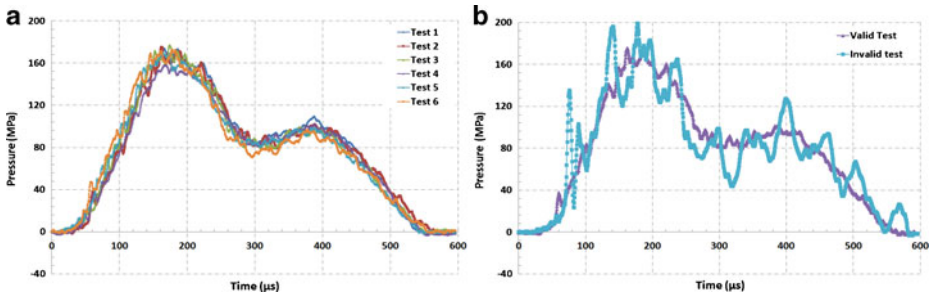

Fig. 11 Pressure history of the chamber with 2.98 mm nozzle at different trials

Recorded pressure profiles from the experiments with different nozzle sizes are compared in Fig. 12. Each graph in this figure is obtained by averaging the accepted test results for each nozzle. The greatest peak pressure, about 200 MPa, was achieved when the nozzle was blocked and there was no water discharge. This value starts decreasing with an increase in the nozzle size as the water discharge volume rises. The lowest peak pressure value corresponds to the 4.02 mm diameter nozzle. The time duration of the elevated pressure inside the chamber was similar for all nozzles. As a result, the time duration of the elevated pressure is largely independent of nozzle size.

A second peak pressure is observed in all of the recorded pressure traces (Fig. 12). From the modelling work described above and from visual evidence using video footage this was due to piston rebound causing a second impact between the piston and the hammer. The magnitude of the second peak pressure is lower than that of the first but it follows the same trend as first peak pressure with respect to changes in the nozzle diameter.

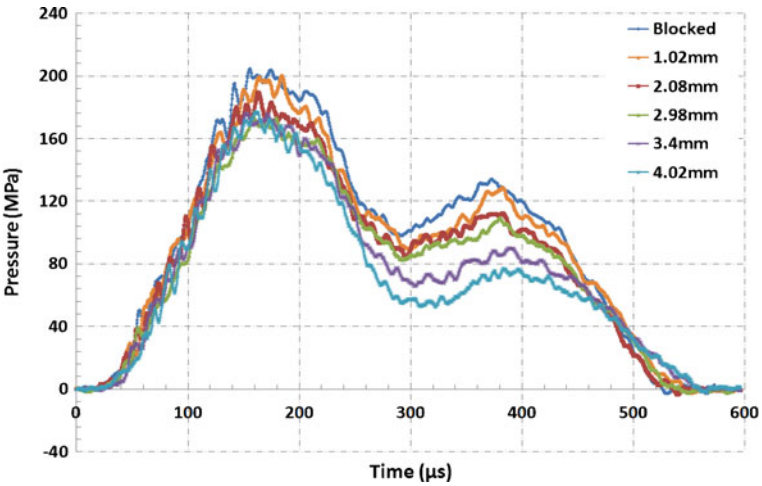

Fig. 12 Comparison of achieved pressure profiles in chamber for five different nozzles

6 Comparison of the Analytical Model with Experimental Results

An excellent correlation was observed between the theoretical pressure profiles and the recorded experimental data (Fig. 13) validating the model.

Figure 14 compares the maximum and minimum pressures from both the experiments and from the modelling for each nozzle size. The error bars in these graphs indicate the range over which the mean pressures fall for all five data points.

The results show that for the smaller nozzles the computational model slightly over predicts the first peak pressure value, but it is in the range of experimental results for the 3.4 and 4.02 mm nozzles.

The minimum pressure before the second impact is estimated fairly accurately for all of the nozzles except for the closed chamber and the 1.02 mm nozzle. The second peak pressure values of the model are all in the ranges of experimental data. The maximum out-of-range error belongs to the computational result of closed chamber with the magnitude of 8%.

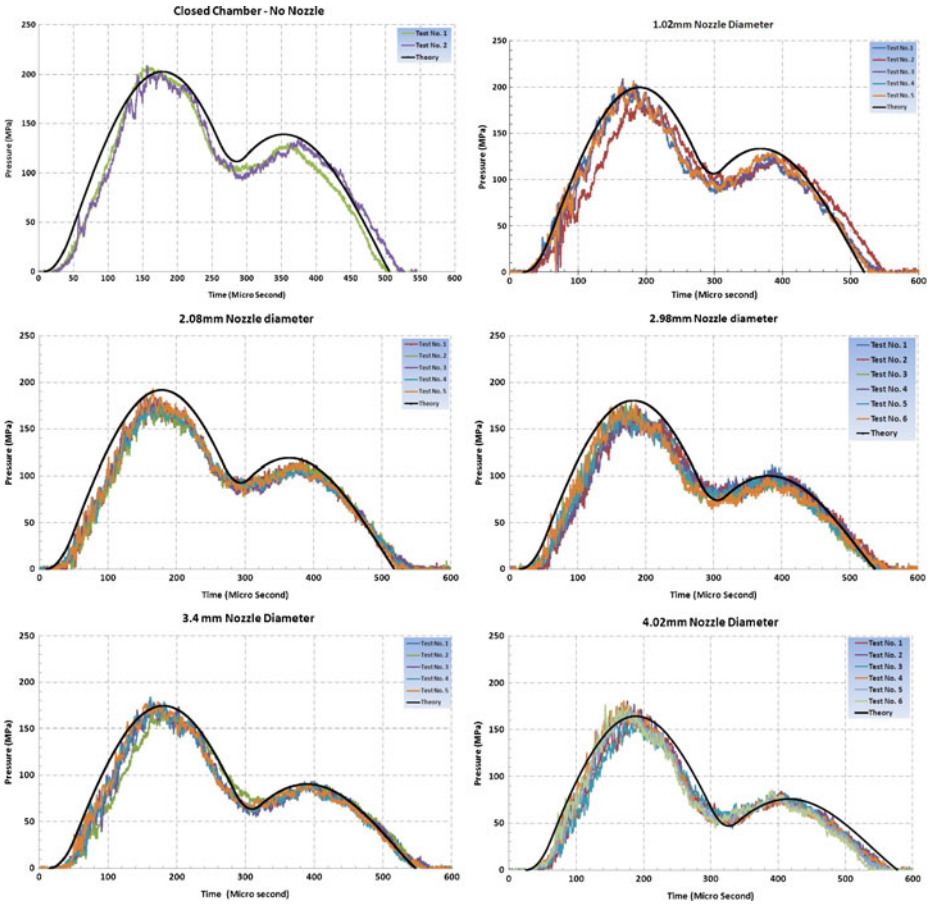

Fig. 13 Comparison of recorded and computational pressure profiles for different tested nozzles; *Solid line* in all graphs is the predicted theoretical pressure profile

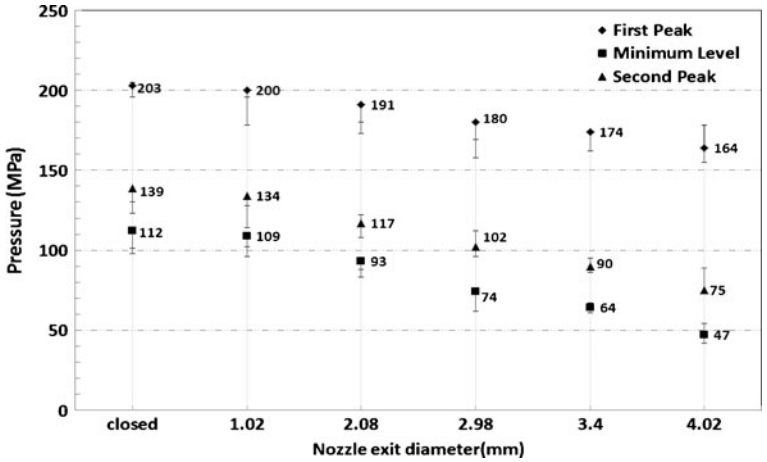

Fig. 14 Comparison of the two maximum and the minimum pressure values obtained experimentally (shown as error bars) and the computational model (shown as data points)

Figure 14 also shows a decrease in the value of these pressures with an increase in the nozzle diameter. The minimum pressure and the second peak pressure fall at a faster rate compared to the first peak pressure. This is because, obviously, the volume of discharge from the chamber increases as the nozzle size increases. Hence the height of the remaining water in the chamber is lower for the second impact with the larger nozzle sizes.

It is apparent that the computational model agrees very well with the experimental data. The model can therefore be used with confidence to determine water pulse parameters such as velocity, volume and shape.

7 Sensitivity to Quasi-Steady-State Flow Assumption

It could be argued that treating the flow as quasi-steady-state is an oversimplification. To address this concern we re-analysed the flow inside the nozzle in non-steady-state. One-dimensional non-steady-state flow assumes that velocity changes with time in the direction of flow between the nozzle entrance and exit ($\frac{\partial u}{\partial t} \neq 0$).

Since the mass of the fluid is constant the relation between the velocity of water at the nozzle inlet and exit can be determined as:

$$v = \frac{m}{A\rho} \quad \overset{m \equiv cte}{\Longrightarrow} \quad \frac{v_1}{v_2} = \frac{A_2\rho_2}{A_1\rho_1} = \frac{{d_2}^2\rho_2}{{d_1}^2\rho_1}$$

thus:

$$\frac{v_1}{v_2} \propto \frac{d_2}{d_1}$$

Based on these assumptions, Eq. 13 is adopted to determine the equivalent length.

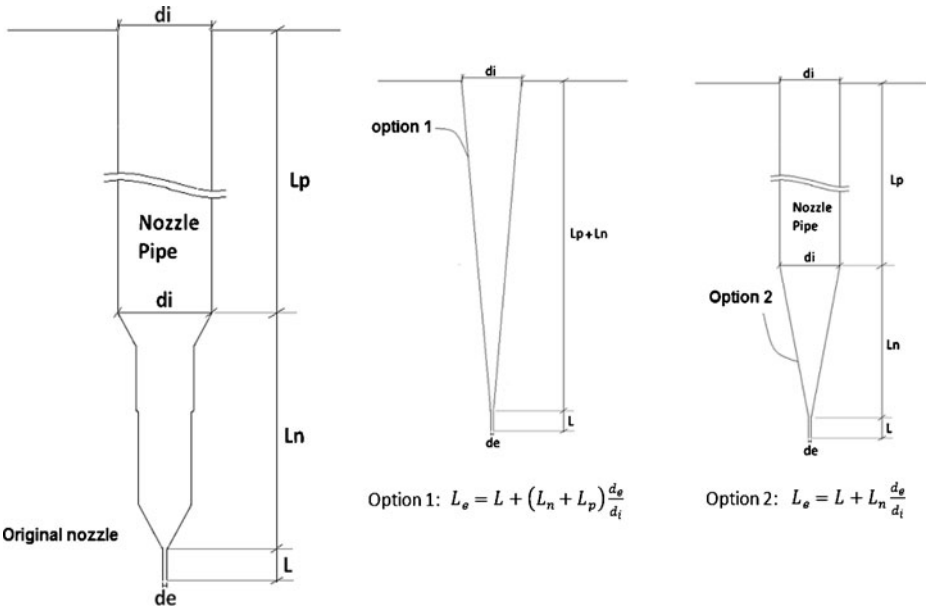

Fig. 15 Internal geometry of the nozzle and nozzle pipe

The geometry of the nozzle used in our apparatus was complex as illustrated in Fig. 15. This geometry consisted of an upstream section L_p, and the main nozzle section, L_n, with a parallel nozzle throat section, L.

In our non-steady-state flow analysis we simplified this nozzle geometry in two different ways, Options 1 and 2 which is shown in Fig. 15. These required the calculation of two different equivalent lengths as described below.

Option 1 in Fig. 15 takes into acount the effect of the upstream section as well as the main nozzle on the pressure and acceleration of the water particles, whilst option 2 concentrates on the main nozzle and assumes that upstream section does not influence the velocity of the fluid. L_e for options 1 and 2 was determined using Eq. 13:

Option 1: $L_e = L + (L_n + L_p)\frac{d_e}{d_i}$
Option 2: $L_e = L + L_n\frac{d_e}{d_i}$

Thus, Eq. 11 is updated for the non-steady-state model as:

$$\int_P^0 \frac{\mathrm{d}P}{\rho} + (1+k)\frac{u^2}{2} + L_e\frac{\partial u}{\partial t} = 0 \tag{23}$$

Results from solving Eqs. 3, 8, 19, 20 and 23 are shown in Figs. 16 and 17 along with the results from the steady-state flow case.

Figure 16 shows that there is no significant difference in pressure between the steady-state and non-steady-state flow cases at the smaller nozzle sizes. For the

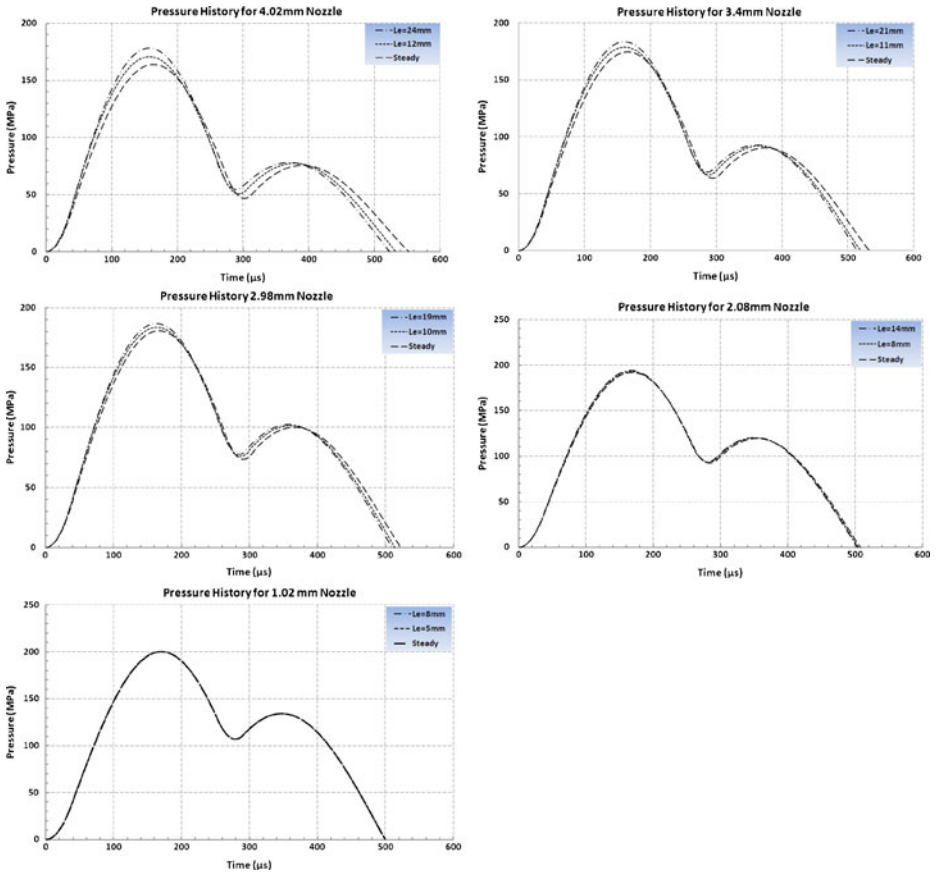

Fig. 16 Comparison of pressure histories for steady-state and non-steady-state model

larger diameter nozzles the calculated pressures are lower for the steady-state flow assumption. The highest pressure is calculated for the nozzle with the longest equivalent length. Further, Fig. 16 shows that the pressure graphs start to climb with a similar gradient, $\frac{\partial P}{\partial t}$, for all three assumptions. However, this gradient starts decreasing faster for steady-state flow model as it approaches the maximum pressure value.

Figure 17 compares the velocity profiles for the steady-state and the non-steady-state models. The results show that the calculated velocity is highest for the steady-state flow model and lowest for the non-steady-state flow model with the larger equivalent length. Also the velocity gradient, $\frac{\partial v}{\partial t}$, for the steady-state flow model is linear at early time whereas it is varying for the non-steady-state flow model, lower initially but then rises until the peak velocities match, or for the larger diameter nozzles, almost match those of the steady-state flow case but at a later time than for the steady-state flow model.

It is interesting to note that the value of the first peak pressure is lower with steady-state flow model, at least with the larger nozzle sizes (Fig. 16); whereas the discharge velocity is highest, and occurs at an earlier time with the steady-state flow

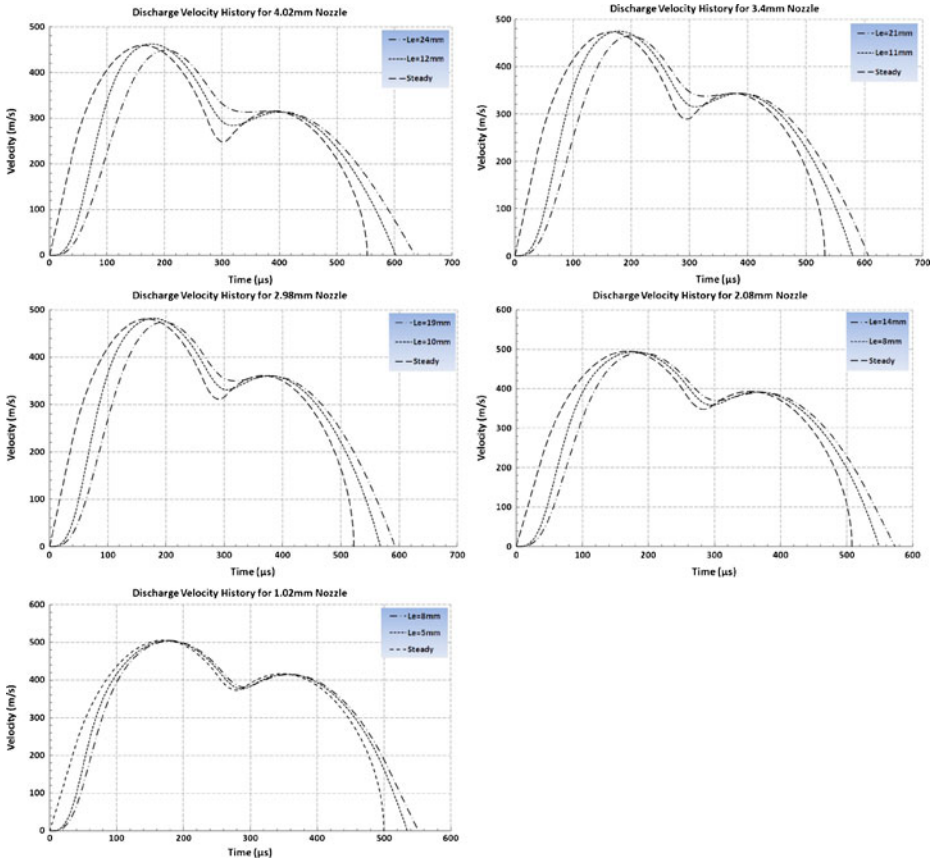

Fig. 17 Comparison of velocity histories for steady-state and non-steady-state model

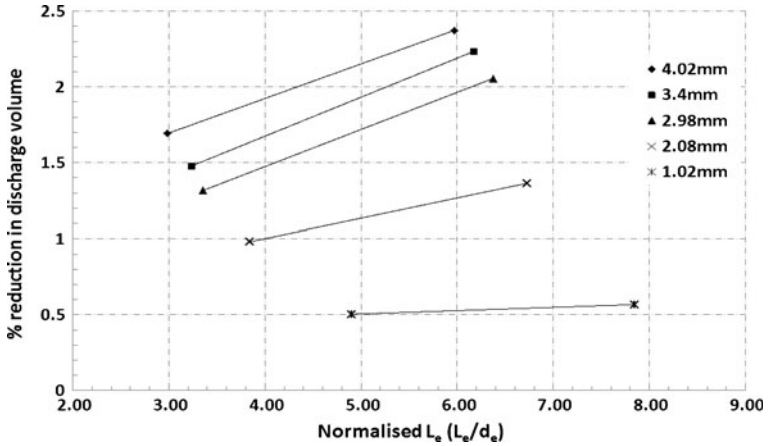

Fig. 18 Change in discharged volume with L_e for different nozzles

model (Fig. 17). This behaviour can be explained by the conservation of energy theorem. The input kinetic energy to the system, governed by the impact velocity of the hammer, is the same for both the steady-state and non-steady-state flow models. This energy converts into a combination of potential energy, increasing pressure in the chamber, and kinetic energy, of the water discharge from the system. The steady-state flow model predicts a higher discharge velocity, and therefore a higher kinetic energy component, up to the first peak; this results in a lower (first) peak pressure with this model.

In summary, reviewing the results of the steady-state and non-steady-state flow models we find that the maximum pressure in the water chamber is somewhat lower for the steady-state flow, although the effect is not large. The influence on the discharge velocity, which was lower for the non-steady-state flow model, was greater and was sensitive to the L_e value. This is important because this velocity profile affects the shape of the water pulse that exits the nozzle.

However, the volume of the water pulse is calculated not to be greatly different between the two models (Fig. 18). For these reasons and because, in the case of the experiments described above, it was difficult to estimate the value of L_e accurately, the steady-state flow model was used when making a comparison with the experimental results.

8 Conclusions

This study has illustrated the mechanism by which high velocity water pulses can be generated using an impacting technique. Furthermore, this new understanding has highlighted those variables that influence the efficiency of generating these water pulses thereby enabling impacting systems of this type to be designed to maximise the efficiency.

A theoretical and computational model explains the impact mechanism and the phenomenon of pressure build-up and release in the water-filled chamber. According to this model, immediately after collision of the hammer and piston, as soon as the piston starts moving, the water inside the chamber compresses and stores energy. As a consequence, the pressure in the chamber rises, triggering the water discharge from nozzle. As water approaches the maximum compression point, determined by the water bulk modulus, the piston slows and eventually stops. This point corresponds to the maximum attainable pressure at the peak compressibility value. From this moment, the compressed water expands elastically releasing the stored energy, lowering the pressure and reversing the direction of the piston's movement. Depending on the system design, at this point often a second collision will take place between the hammer and piston. This causes the piston to change direction again and recompress the water inside the chamber. A second peak pressure is then recorded, the magnitude of which is related to the compressibility of the remaining volume of water in the chamber.

This model was used to design an impacting system which was used to conduct experiments using five nozzles with diameters of: 1.02 mm, 2.08 mm, 2.98 mm, 3.43 mm and 4.02 mm. The data from the pressure sensor mounted in the cylindrical chamber showed two peak values, the second being lower than the first. The magnitude of these maximum pressures decreased with increasing nozzle size. The

first peak pressure with the 1.02 mm nozzle had a magnitude of 200 MPa; this value was reduced to 170 MPa whilst with the 4.02 mm nozzle. The discharge velocity history at the nozzle exits with the different diameter nozzles followed the same trend with the highest peak velocities of 500 m/s for the 1.02 mm and of 460 m/s for the 4.02 mm nozzle.

The model was developed using the assumption of steady-state flow. Although the values achieved seemed reasonable and corresponded well with experimental results there was a concern that this assumption oversimplified the problem. Consequently, further analysis was conducted and a more complex non-steady-state flow model was developed. In this new model the concept of equivalent length, L_e, which has also been used by [10], was employed. This equivalent length factor, which takes into account the inertial effect of the nozzle, was found to be influential in the resultant pressure and discharge velocity gradients. Increases in L_e increased the critical pressure points whilst decreasing the critical velocity points. This nozzle discharge velocity was found to be more sensitive to changes in L_e than the calculated pressure values. The influence of the L_e value was found to be greater for the larger nozzle sizes.

Although, the discharge velocity was significantly affected by the L_e value, the volume of the generated water pulse was almost unchanged.

In summary, the additional complexity of the non-steady-state flow model was found not to be warranted particularly considering the sensitivity of this non-steady-state system to the value of L_e and the fact that the methods available to calculate the value of L_e are imprecise. Hence the steady-state flow approach was preferred.

Acknowledgements The authors would like to thank CRCMining for financial support of the project; Dr Zongyi Qin for sharing his knowledge to understand the fundamentals of the phenomenon; Mr Joji Quidim for his skilful support in preparing the electronics and data acquisition system, Mr Allan Boughen for his assistance in conducting the experiments.

References

1. Edney, B.: Experimental studies of pulsed water jets. In: 3rd International Symposium on Jet Cutting Technology, pp. B2:11–B2:26 (1976)
2. Vijay, M.M., Foldyna, J., Remisz, J.: Ultrasonic modulation of high-speed water jets. In: Proceeding of International Conference Geomechanics 93 Rotherham, pp. 327–332 (1993)
3. Foldyna, J., Sitek, L., Svehla, B., Svehla, S.: Utilization of ultrasound to enhance high-speed water jet effects. Ultrason. Sonochem. **11**, 131–137 (2004)
4. Nebeker, E.B., Rodriguez, S.E.: Percussive water jets for rock cutting. In: 3rd International Symposium on Jet Cutting Technology, pp. B1:1–B1:9 (1976)
5. Chahine, G.L., Conn, A.F., Johnson, V.E.: Cleaning and cutting with self-resonating pulsed water jets. In: 2nd U.S. Water Jet Symposium, pp. 238–253 (1983)
6. O'Keefe, J.D., Wrinkle, W.W., Scully, C.N.: Supersonic liquid jets. Nature **213**(5071), 23–25 (1967)
7. Pianthong, K., Zakrzewski, S., Behnia, M., Milton, B.E.: Supersonic liquid jets: their generation and shock wave characteristics. Shock Waves **11**, 457–466 (2002)
8. Pianthong, K., Zakrzewski, S., Behnia, M., Milton, B.E.: Characteristics of impact driven supersonic liquid jets. Exp. Fluid Sci. **27**, 589–598 (2003)
9. Matthujak, A., Pianthong, K., Sun, M., Takayama, K.: Experimental study of impact-generated high-speed liquid jet. In: The 21st Conference of Mechanical Engineering Network of Thailand (2007)
10. Rehbinder, G.: Investigation of water jet pulses generated by an impact piston device. Appl. Sci. Res. **40**, 7–37 (1983)

11. Ridah, S.: Shock waves in water. J. Appl. Phys. **64**(1), 152–158 (1988)
12. Igra, D., Takayama, K.: Numerical simulation of shock wave interaction with water column. Shock Waves **11**, 219–228 (2001)
13. Grinenko, A., Gurovich, V.T., Krasik, Y.E., Sayapin, A., Efimov, S., Felsteiner, J.: Analysis of shock wave measurements in water by a piezoelectric pressure probe. Rev. Sci. Instrum. **75**(1), 240–244 (2004)
14. Li, Y.H.: Equation of state of water and sea water. J. Geophys. Res. **72**(10), 2665–2678 (1967)
15. Bridgeman, P.W.: The physics of high pressure. London (1949)
16. Fox, R.W., Pritchard, P.J., McDonald, A.T.: Introduction to fluid mechanics, 7th edn. Don Fowley (2009)
17. Soutas-Little, R.W., Inman, D.J., Balint, D.S.: Engineering Mechanics: Dynamics, Computational Edition, SI edn. Cengage Learning, Toronto, ON (2009)
18. Chatterjee, A., Ruina, A.L.: Two interpretations of rigidity in rigid-body collisions. J. Appl. Mech. **65**(4), 894–901 (1998)